PHYSICAL REVIEW A VOLUME 43, NUMBER 5 1 MARCH 1991

Field-ionization Stark spectra of Ba Rydberg atoms at high density of states

A. König, J. Neukammer,* H. Hieronymus, and H. Rinneberg*
Institut für Atom- und Festkörperphysik, Freie Universität Berlin, Arnimallee 14, 1000 Berlin 33, Germany

(Received 22 May 1990)

Stark spectra of barium Rydberg states above the classical field-ionization limit have been recorded at high density of states employing high-resolution laser spectroscopy. The spectra, taken at a binding energy of about $\varepsilon \approx -55$ cm^{-1} with respect to zero-field threshold and at electric-field strengths $F \approx 100$ V/cm exhibit dramatic variations in line profiles with increasing external field strength. The WKB quantum-defect theory of the Stark effect of nonhydrogenic atoms was used to analyze the recorded spectra, and excellent agreement between measured and calculated line profiles was achieved. Core-induced coupling of closed and open hydrogenic Stark channels was found to contribute dominantly to the linewidth of the recorded Stark resonances. In addition, a reformulation of this theory by McNicholl, Ivri, and Bergeman (unpublished) in terms of a configuration-interaction model was employed to analyze a particular avoided crossing of several Stark components. In this way recorded line profiles were parametrized within a limited model to obtain resonance energies, linewidths, and Fano q parameters.

I. INTRODUCTION

Within the last decade the Stark effect of nonhydrogenic atoms has been investigated extensively, both experimentally and theoretically.[1] In particular, Rydberg states of alkali-metal and alkaline-earth atoms have been studied below[2-4] and above[5-7] the classical field-ionization limit by means of laser spectroscopy. In nonhydrogenic atoms, non-Coulombic parts of the potential result in core-induced coupling of hydrogenic Stark channels. This mixing manifests itself, e.g., in avoided crossings of quasibound Stark components.[2] Furthermore, above the classical field-ionization limit, the mixing of quasistable and field-ionizing Stark channels causes an additional decay process leading to Fano profiles in the absorption cross section of Stark resonances.[7] In particular, close to the classical field-ionization limit, the core-induced coupling causes highly nonmonotonic field-ionization rates at avoided crossings of Stark components.[8] Furthermore, stabilization of field-ionization Stark components occurs at avoided crossings if a destructive interference exists in decay amplitudes to open Stark channels. Dramatically reduced linewidths[9] and anomalously long lifetimes[10] have been observed and explained in this way.

Extending a Wentzel-Kramers-Brillouin (WKB)-solution of the hydrogenic Stark problem[11] by including field-independent quantum-defect parameters, Harmin has given a nonperturbative theoretical description of the Stark effect of nonhydrogenic atoms with spherically symmetric ionic core. He has applied this theory to calculate photoionization cross sections of sodium in external electric fields[12] and has achieved excellent agreement between theoretical and experimental[6] spectra. This theory has recently been generalized to include configurations with nonspherical (excited) ionic cores.[13] These theories do not require any parameters to calculate photoionization cross sections apart from zero-field multichannel quantum-defect (QD) parameters and zero-field transition dipole matrix elements.

A different approach to describe Stark spectra of nonhydrogenic atoms above the classical field-ionization limit[4,14] is based on configuration-interaction theory of autoionizing atomic states,[15] by identifying closed Stark channels with bound atomic states while open channels are taken as continua. Recently McNicholl *et al.*[14] have reformulated the WKB-QD Stark theory[12] in terms of configuration-interaction theory. By comparing corresponding expressions for the photoionization cross section, parameters entering configuration-interaction theory such as (complex) Hamiltonian matrices, transition moments to modified bound states, Fano q parameters, and background amplitudes are theoretically accessible. By diagonalizing the complex Hamiltonian matrix, resonance energies and linewidths can be deduced for Stark components, i.e., modified bound states.

In this paper we report high-resolution Stark spectra of barium Rydberg states above the classical field-ionization limit. Apart from a recent study of helium Stark spectra,[16] our measurements were taken at considerably higher density of states compared to previous investigations of the Stark effect above the field-ionization limit. Because of the small electric fields applied, tunneling can be neglected and core-induced coupling provides the dominant mechanism to the observed linewidths. Although Rydberg series of barium converging towards the first threshold are perturbed by many doubly excited configurations, none of such perturbing states falls into the energy range covered by our experiments. Therefore we have used Harmin's theory in its original form to analyze our spectra, and it was found to provide an excellent description of the recorded photoionization cross sections at high density of states. In addition, we have applied configuration-interaction theory to one particular multiple crossing of Stark states to obtain resonance energies and linewidths as a function of applied field strength. Several interference minima in linewidths are clearly discernible.

II. EXPERIMENT

In Fig. 1 the experimental setup used to excite Stark components of barium Rydberg states above the classical field-ionization limit is shown. Starting from the $6s^2\,{}^1S_0$ ground state, Stark components were reached via the $6s6p\,{}^1P_1$ $m=0$ intermediate level employing two continuous wave (cw) dye lasers. The lasers were operated with rhodamine 110 and stilbene 3 as dyes and stabilized to a bandwidth of about 1 MHz. Both laser beams counterpropagated and intersected a well-collimated beam of barium atoms perpendicularly at the center of a parallel plate capacitor. The polarization vectors of both linearly polarized laser beams coincided with the direction of the electric field. The capacitor was made from two 0.6-cm-thick brass plates with a diameter of 14 cm, being 1.98 cm apart. Two central holes ($d\approx 0.6$ cm) allowed the atomic beam to pass. A dc-voltage was applied symmetrically with respect to the ground to the upper and lower plate, thus minimizing field inhomogeneities inside the excitation volume. In order to further reduce the influence of field inhomogeneities in the direction of the applied electric field, the laser beams were focused down to a beam waist of about $2w_0\approx 80$ μm. Excitation of barium Stark components was monitored by counting Ba$^+$ ions, which were detected by a (shielded) channel electron multiplier situated outside the parallel plate capacitor. The multiplier output signals were processed using standard counting electronics. Field ionization occurring within the excitation volume contributed to the production of Ba$^+$ ions. In addition, for Stark components with low field-ionization rates, collisions with barium atoms in the $6s^2\,{}^1S_0$, $6s6p\,{}^1P_1$, or metastable $5d6s\,{}^{1,3}D$ states as well as field ionization outside the parallel plate capacitor were responsible for the signals observed.[17] Spectra were recorded by scanning the wavelength of the second dye laser ($\lambda_2\approx 418$ nm) keeping the first laser tuned to the transition $6s^2\,{}^1S_0\rightarrow 6s6p\,{}^1P_1$ ($\lambda_1=553.702$ nm). A reference experiment (see Fig. 2) served to actively stabilize the first laser to the Ba resonance line by monitoring the fluorescence emitted from the $6s6p\,{}^1P_1$ intermediate level. Furthermore, the setup shown in Fig. 2 was used to record zero-field spectra of $6sns\,{}^1S_0$ and $6snd\,{}^1D_2$ Ba Rydberg states (cf. Fig. 3). Stark spectra were recorded simultaneously with zero-field spectra, which provided an accurate absolute energy scale, since zero-field energies of barium Rydberg states are known with high precision.[17] Small stray electric fields present in the excitation volume were compensated by means of the parallel plate capacitor shown in the

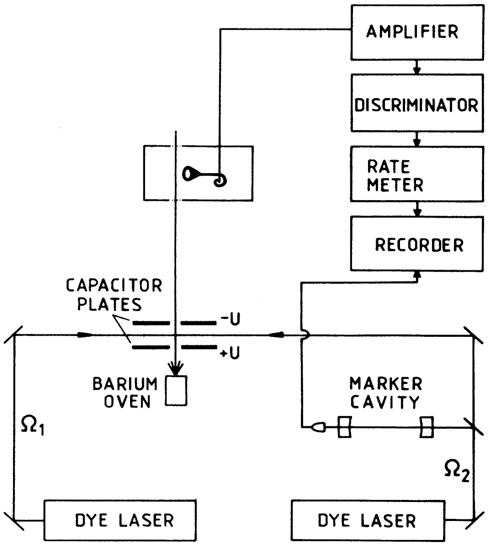

FIG. 1. Experimental setup for Stark spectra of Ba Rydberg states. Ba$^+$ ions, produced by the decay of Stark components, were counted by means of a channel electron multiplier.

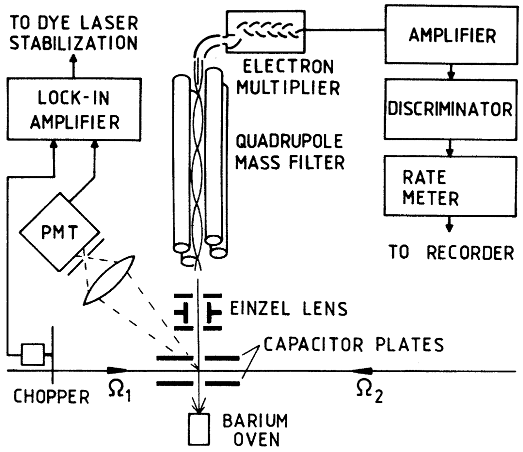

FIG. 2. Zero-field reference experiment for frequency calibration and active stabilization of the wavelength of the first dye laser. The abbreviation PMT stands for photomultiplier tube.

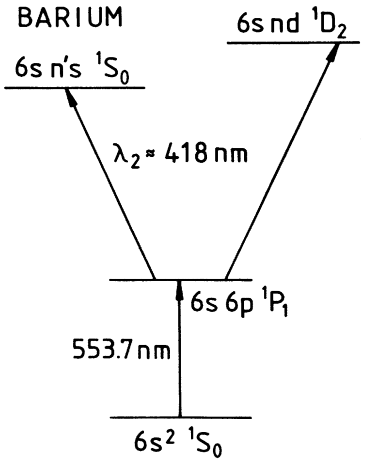

FIG. 3. Excitation scheme in zero electric field.

lower part of Fig. 2. Again, excitation of Ba Rydberg states was monitored by counting Ba^+ ions using a quadrupole mass spectrometer. The mass filter was operated without dc voltage, thus serving as a drift tube only. Interpolation by means of a marker cavity with a free spectral range of 149.75 MHz allowed us to determine energy separations with an accuracy of ± 20 MHz. A Burleigh wave meter served to measure the wavelengths of the laser radiations. In zero electric field a spectral resolution of about 10 MHz full width at half maximum (FWHM) was achieved with both experimental setups. The field strength inside the excitation volume (see Fig. 1) was reduced by about 3% compared to that expected for an ideal parallel plate capacitor because of the central hole in the upper and lower capacitor plate. Therefore, an absolute field calibration was achieved by comparing experimentally observed line profiles, which strongly depend on the applied field strength with calculated spectra (see below). Electric field strengths were estimated in this way to vary by at most ± 0.02 V/cm within the excitation volume (see Fig. 1). This is consistent with the degree of misalignment of both capacitor plates. Furthermore, from principal quantum numbers of the highest Rydberg states resolved in zero-field spectra we estimate stray electric fields to be in the order of a few mV/cm in both experimental setups.

III. THEORETICAL BACKGROUND

A. WKB quantum-defect theory

The WKB quantum-defect formalism of the Stark effect of nonhydrogenic atoms[12] will be used to analyze our experimental spectra, pertaining to the energy range between the classical field-ionization limit and the zero-field threshold. In its original form, the WKB-QD theory requires a spherically symmetric ionic core as found in alkali metals and alkali-metal-like atoms.[12] Because of its two valence electrons and the low-lying $5d$ orbitals of Ba^+, this requirement is generally not met in barium. However, as will be discussed in the next section, the original WKB-QD theory is sufficient to analyze our experimental data, since they cover a narrow energy and electric-field range only. The short outline of Harmin's theory, given below, is intended to provide the theoretical background for the discussion of our experimental results (cf. Sec. IV).

A description of nonhydrogenic atoms within the framework of quantum-defect theories (QDT) is accomplished by dividing the range of the radial coordinate r of the valence electron into a core region ($r \leq r_0$) and a region ($r \geq r_0$), where a pure hydrogenic potential exists. For $r \geq r_0$ the effect of the atomic core is taken into account by phase shifts $\delta_l = \pi\mu_l$ being independent of external fields because of the strong intra-atomic forces prevailing in the core region. In the absence of an external field the QDT wave function can be written as

$$\Psi_{\epsilon l m}(\mathbf{r}) = (\cos\delta_l) f_l(\mathbf{r}) - (\sin\delta_l) g_l(\mathbf{r}) , \tag{1}$$

where

$$f_l(\mathbf{r}) = f_{\epsilon l}(r) Y_{lm}(\theta,\phi) , \tag{2}$$

$$g_l(\mathbf{r}) = g_{\epsilon l}(r) Y_{lm}(\theta,\phi) . \tag{3}$$

Here $f_{\epsilon l}(r)$ and $g_{\epsilon l}(r)$ represent a radial base pair of regular and irregular Coulomb wave functions. It is well known that the hydrogenic Stark problem is separable in parabolic coordinates $\mathbf{r} = (\xi,\eta,\phi)$ resulting in solutions $\psi_{\epsilon\beta m}(\mathbf{r})$ and $\chi_{\epsilon\beta m}(\mathbf{r})$ being regular and irregular at $\eta = 0$. These solutions are characterized by the total energy ε and quantum number m representing the projection of the angular momentum onto the field axis. The parameter β describing the fractional charge associated with the bound ξ motion is uniquely defined by the parabolic quantum number n_1 at a given energy ε. In contrast to the ξ coordinate the motion in η is always open, with tunneling occurring below the critical parabolic energy, $\varepsilon_c = -4\ \mathrm{Ry} \times \sqrt{(1-\beta)F/F_0}$. However, because of the low electric-field strengths ($F \leq 100$ V/cm) considered in this paper, the maximum of the combined Coulomb-Stark potential in the η coordinate is very broad. Therefore, except for a narrow energy range in the vicinity of the critical parabolic energy ε_c, tunneling is negligible, and the opening of closed channels occurs abruptly when increasing energy or electric-field strength. In the remaining part of this paper we designate hydrogenic n_1 channels below their critical parabolic energy as being closed with resonance energies ε_{n_1}, and channels above this energy as being open. In the region $r_0 \leq r \ll a_0(F/F_0)^{-1/2}$, where the Coulomb part of the potential outweighs the Stark term, parabolic and spherical solutions are connected by a field-dependent nonunitary transformation $U = U^F$:

$$f_l(\mathbf{r}) = \sum_{\beta} [(U^F)^{-1}]_{l\beta} \psi_{\epsilon\beta m}(\mathbf{r}) , \tag{4}$$

$$g_l(\mathbf{r}) = \sum_{\beta} \tilde{U}^F_{l\beta} \csc\gamma^F_{\beta} \chi_{\epsilon\beta m}(\mathbf{r}) , \tag{5}$$

where γ^F_{β} is a field-dependent asymptotic phase shift between regular and irregular wave functions in the η coordinate.[12] Atomic units for length and field strength are denoted by a_0 and F_0, respectively.

For nonhydrogenic atoms a quantum-defect solution in spherical coordinates $\Psi_{\epsilon l m}(\mathbf{r})$, applicable to the region $r_0 \leq r \ll a_0(F/F_0)^{-1/2}$, can be obtained in terms of (hydrogenic) parabolic solutions by inserting the hydrogenic regular and irregular solutions [cf. Eqs. (4) and (5)] into the expression given in Eq. (1). In contrast to $\psi_{\epsilon\beta m}(\mathbf{r})$, the wave function obtained in this way is made up from different hydrogenic solutions, representing a coupling of different n_1 channels. Since the transformation U^F is nonunitary, the wave functions $\Psi_{\epsilon l m}(\mathbf{r})$ have to be orthonormalized by calculating the density of states (DOS) matrix D^F with matrix elements $D^F_{l'l} = (\langle \Psi' | \Psi \rangle^{-1})_{l'l}$. In matrix notation the density of states matrix can be expressed as

$$D^F = \sec\delta[\tilde{Q}(H^F)^{-1}Q + (\tan\delta)H^F(\tan\delta)]^{-1}\sec\delta , \tag{6}$$

where the matrices H^F and Q are given by

$$H^F = \tilde{U}^F U^F \ , \tag{7}$$

$$Q = 1 - \tilde{U}^F \cot\gamma_\beta^F U^F \tan\delta \ . \tag{8}$$

The matrix H^F represents the hydrogenic density of states matrix, and the trigonometric functions [see Eqs. (6) and (8)] correspond to diagonal matrices. It should be noted that apart from a trivial factor (π^{-1}) the diagonal matrix $\tan\delta$ represents the K matrix if configurations with a spherically symmetric core are taken into account only. For atoms, such as barium, for which configuration interactions exist below the first threshold, the K matrix and its diagonal form ($-\pi^{-1}\tan\delta$) are connected by a frame transformation ($U_{i\alpha}$).[13] The absorption cross section in the presence of an external electric field can be expressed in terms of zero-field absorption cross sections and the density-of-states matrix. In matrix notation one obtains

$$\sigma^F(\varepsilon) = \mathrm{Tr}[D^F \sigma^{F=0}(\varepsilon)] \ , \tag{9}$$

where the elements of the absorption cross section matrix $\sigma^{F=0}(\varepsilon)$ are given by

$$\sigma_{l'l}^{F=0}(\varepsilon) = 4\pi^2 \alpha\hbar\omega R_{l'}^0 , R_l^{0*} \ . \tag{10}$$

In Eq. (10) $R_l^0 = \langle i | r_q | \Psi_{\epsilon l m} \rangle$ is a zero-field transition dipole matrix element and $|i\rangle$ denotes the initial state of the atom involved in the photoexcitation process. The component r_q depends on the polarization of the exciting radiation. Equation (9) may be interpreted as a two-step process, where the second factor describes the photoexcitation proper of a spherical component $\Psi_{\epsilon l m}$. This excitation occurs close to the atomic core since $|i\rangle$ is concentrated in that region. The density-of-states matrix accounts for a probability redistribution onto the various outgoing parabolic (n_1) channels.

We conclude this section by illustrating the density-of-states matrix (see Fig. 4) of barium at an external field strength of $F = 97.60$ V/cm and for energies in the vicinity of the zero-field energy of the $6s47d\ ^1D_2$ Rydberg state. The energies and field strengths chosen fall within the range of energies and field strength covered by our experimental spectra, to be discussed in the following sections. Furthermore, approximations made in calculating the matrix elements $D_{l'l}^F (0 \le l', l \le 2)$ shown in Fig. 4 will be discussed in Sec. IV, where a comparison of calculated and observed photoionization cross sections will be given. As can be seen from Fig. 4, the matrix elements $D_{l'l}^F$ show pronounced resonances whose linewidths are caused by core-induced coupling between closed and open hydrogenic channels. Apart from one channel with $n_1 = 6$, which is close to its parabolic field-ionization threshold, in hydrogen the corresponding resonances exhibit vanishing linewidths, since these resonances are strongly bound. Deviations of the density-of-states matrix D^F (see Fig. 4) from the unity matrix at the resonance energies are caused by the external electric field. It follows from Eq. (9) that only D_{00}^F, D_{02}^F, and D_{22}^F contribute to the photoabsorption cross section when exciting Stark resonances ($m = 0$) starting from the $6s6p\ ^1P_1$ intermediate level.

B. Configuration-interaction formalism

The core-induced coupling between closed and open hydrogenic channels occurring above the classical field-

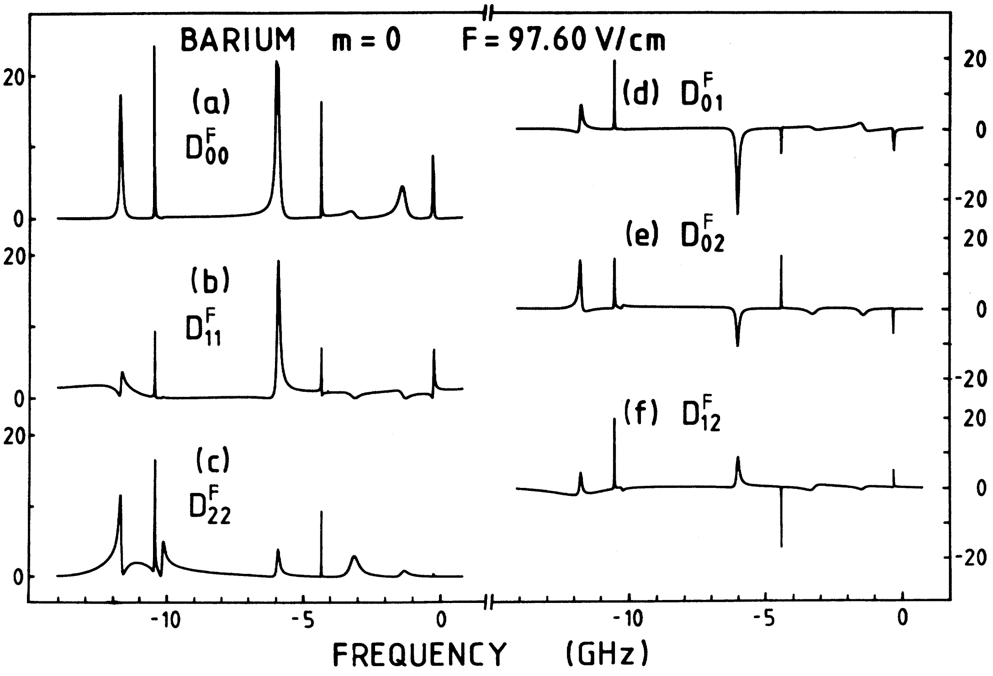

FIG. 4. Density-of-states matrix elements $D_{l'l}^F$ $(0 \le l', l \le 2)$ in the vicinity of the zero-field energy of the $6s47d\ ^1D_2$ Rydberg state, chosen as origin of the frequency scale.

ionization limit in nonhydrogenic atoms can be treated within the framework of configuration-interaction theory. Following the pioneering work of Fano, Mies has extended the description of autoionization to N resonances and M continua.[15] More recently, Liu *et al.*[9] and McNicholl *et al.*[14] have reformulated the WKB-QD theory of the Stark effect of nonhydrogenic atoms to allow a direct comparison with configuration-interaction theory. We follow this approach,[14] starting from the following equation for the photoabsorption cross section:

$$\begin{aligned}\sigma(\varepsilon)=4\pi^2\alpha\hbar\omega(R_c(\varepsilon)\tilde{R}_c(\varepsilon)-(1/\pi)\\ \times\mathrm{Im}\{[R_d(\varepsilon)-i\pi R_c(\varepsilon)\tilde{V}(\varepsilon)]\\ \times[\varepsilon-h^c(\varepsilon)]^{-1}\\ \times[\tilde{R}_d(\varepsilon)-i\pi V(\varepsilon)\tilde{R}_c(\varepsilon)]\})\ .\end{aligned} \tag{11}$$

The $N\times M$ matrix $V(\varepsilon)$ in Eq. (11) represents the coupling between the N discrete states and the M continuum channels. This coupling contributes to the imaginary part of the complex $N\times N$ matrix

$$h^c(\varepsilon)=H(\varepsilon)-i\pi V(\varepsilon)\tilde{V}(\varepsilon)=H(\varepsilon)-i\Gamma/2\ .$$

The real part of $h^c(\varepsilon)$ refers to the N modified bound states, $R_d(\varepsilon)$ denotes the transition moment (row vector) between the initial atomic state $|i\rangle$ and the N modified bound states, whereas the row vector $R_c(\varepsilon)$ contains the transition moments to the M continuum channels. Equation (11) is identical to expression (2.26) of Ref. 14 and is closely related to expressions given by Mies.[15] By defining the Fano q parameters[14,15]

$$q_i=(R_d)_i\Big/\left[\pi\sum_{j=1}^{M}V_{ij}(R_c)_j\right],\quad i=1,2,\ldots N$$

Eq. (11) can be cast in the following form:

$$\sigma(\varepsilon)=4\pi^2\alpha\hbar\omega\left[R_c(\varepsilon)\tilde{R}_c(\varepsilon)-\pi^{-1}\sum_{i,j}\left[\frac{(R_d)_i(R_d)_j}{q_iq_j}((q_iq_j-1)\{\mathrm{Im}[\varepsilon-h^c(\varepsilon)]^{-1}\}_{ij}-(q_i+q_j)\{\mathrm{Re}[\varepsilon-h^c(\varepsilon)]^{-1}\}_{ij})\right]\right]\ , \tag{12}$$

where the background amplitude $R_c\tilde{R}_c$ is given by

$$R_c(\varepsilon)\tilde{R}_c(\varepsilon)=\sum_{i,j}(R_d)_i(R_d)_j\left[\left[\frac{\Gamma}{2}\right]^{-1}\right]_{ij}\Big/(\pi q_iq_j)\ . \tag{13}$$

For $N=M=1$, Eqs. (12) and (13) reduce to the well-known expressions reported by Fano.[15] By identifying open hydrogenic n_1 channels with continuum states of the configuration-interaction model and by taking bound Stark states as discrete basis states, a direct comparison of the expression for the photoionization cross section of the reformulated WKB-QD theory[9,14] with the expression given in Eq. (11) or Eq. (12) is possible. In this way the complex matrix $h^c(\varepsilon)$, the background amplitude $R_c(\varepsilon)\tilde{R}_c(\varepsilon)$, as well as the transition moment $(R_d)_i$ and the q parameter q_i associated with each of the modified bound states can be calculated using the WKB-QD formalism. By taking hydrogenic Stark functions as basis states for the matrix $h^c(\varepsilon)$, the elements of the configuration-interaction matrix $V(\varepsilon)$ are due to core-induced coupling of open and closed Stark channels only.

IV. RESULTS AND DISCUSSION

In this section we compare experimental spectra of barium Stark components recorded above the classical field-ionization limit with absorption cross sections calculated as a function of energy. Spectra were taken over the limited range $-56.78\leq\varepsilon\leq-55.94$ cm^{-1} of binding energies ε and external field strengths $92.68\leq F\leq 97.98$ V/cm. This energy range corresponds to effective principal quantum numbers $43.96\leq\nu\leq 44.29$, where $\nu=[(2\text{ Ry})/(-2\varepsilon)]^{1/2}$. The rectangular area shown in Fig. 5 illustrates the energy and the electric-field region covered by our experiments. In addition, spectra were taken at constant electric-field strength $F=97.88$ V/cm starting from $\varepsilon=-59.74$ cm^{-1} up to $\varepsilon=-45.74$ cm^{-1}, indicated by the vertical bar in Fig. 5. The heavy line denotes the classical field-ionization limit $F_c=\frac{1}{4}F_0[\varepsilon/(2\text{ Ry})]^2$. Furthermore, the linear Stark effect of the hydrogenic Stark manifolds with $n=40$, 45, and 50 is illustrated in Fig. 5. As can be seen, at $\varepsilon\approx-60$ cm^{-1} the uppermost and lowermost components of the $n=40$ and 50 manifolds cross, corresponding to a value of $3(F/F_0)n^5\approx 10$, indicating strong n mixing at the clas-

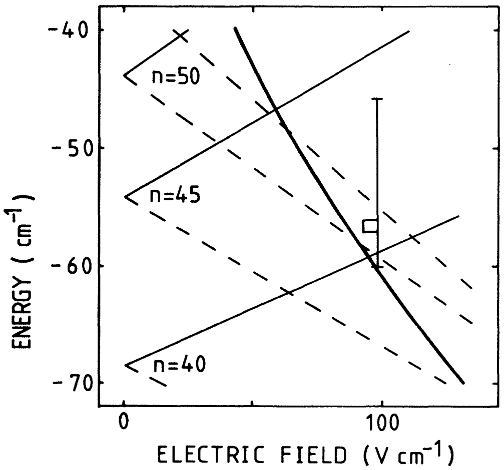

FIG. 5. Linear Stark splitting of the hydrogenic manifolds $n=40$, 45, and 50. The heavy line corresponds to the classical field-ionization limit. The rectangular area and vertical bar indicate the energy and electric-field range covered by the experiments.

sical field-ionization limit. A rough estimate for the total density ρ of hydrogenic Stark components ($m=0$) per unit energy interval is obtained by multiplying this value with the average density $(n/3Fn^2)[F_0/(2\text{ Ry})]$ of a Stark multiplet in a linear approximation, yielding $\rho=n^4/(2\text{ Ry})$. It follows that about 20 Stark components are expected to fall within the energy range of about 1 cm^{-1} covered by the experimental spectra taken at different electric-field strengths. For illustration, in Fig. 6 we show resonance energies ε_{n_1} of quasibound hydrogenic Stark components in the energy ($-56.78\le\varepsilon\le-55.94\text{ cm}^{-1}$) and field ($95\le F\le 98$ V/cm) range under consideration, calculated within the WKB formalism.[11] To facilitate comparison with experimental and calculated data for barium we have chosen the zero-field energy of the $6s47d\,^1D_2$ Rydberg state of barium as origin of the vertical axis in Fig. 6. Because of the limited field range the shift of hydrogenic Stark components, designated by their (parabolic) quantum numbers (n,n_1) is linear to a good approximation. Within the energy and electric-field range of Fig. 6, parabolic channels with $n_1\le 3$ are open, whereas those with $n_1\ge 7$ are strongly bound. The energy range covered in Fig. 6 corresponds to about twice the splitting $3Fn[(2\text{ Ry})/F_0)]$, i.e., 16 GHz, between adjacent Stark components (n,n_1,n_2) and (n,n_1-1,n_2+1) belonging to the same principal quantum number. The quasiperiodicity of the Stark pattern with increments in energy of about 16 GHz is evident. A similar field dependence as for hydrogen is expected for the Stark components of barium Rydberg states. However, the separability of the Schrödinger equation in parabolic coordinates is no longer strictly valid, resulting in a core-induced coupling between different n_1 channels. Besides causing small energy shifts compared to hydrogenic Stark components, this coupling results in avoided crossings between quasibound Stark components. Furthermore, because of the coupling to open n_1 channels, Stark components which otherwise would be quasibound acquire continuum character, i.e., autoionize. Our experimental data provide striking examples for these effects.

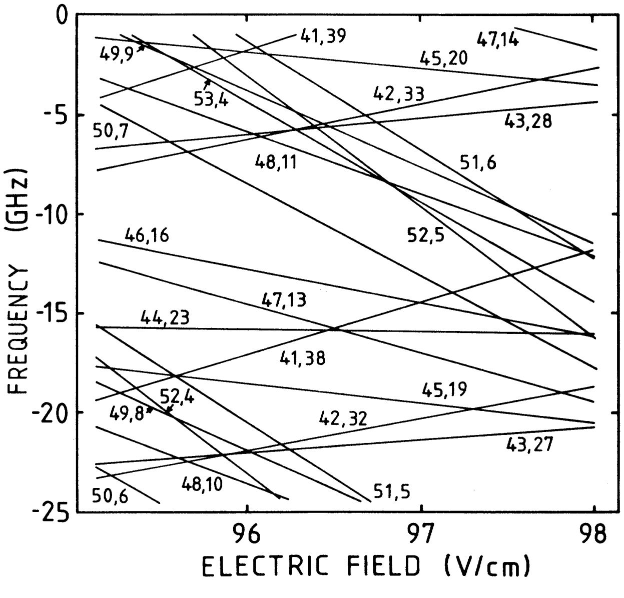

FIG. 6. Hydrogenic ($m=0$) Stark energy levels ε_{n_1} referred to the zero-field energy of the $6s47d\,^1D_2$ Ba Rydberg state. Stark components (n,n_1) with field-ionization linewidth $\Gamma_{n_1n_1}\le 5$ GHz are included only.

A. WKB quantum-defect analysis of experimental spectra

In the following we discuss the analysis of the experimental spectra employing the WKB-Qd theory of the Stark effect in nonhydrogenic atoms.[12] In Figs. 7 and 8 we compare experimental spectra (left-hand side) with calculated (relative) cross sections (right-hand side). Again, we have chosen the energy of the $6s47d\,^1D_2$ Rydberg state in zero electric field as origin of the frequency scale. Each experimental trace illustrated in Figs. 7 and 8 represents the ion count rate in arbitrary units recorded as a function of frequency of the second dye laser. Since all spectra were recorded under similar conditions, the vertical scales of all traces are essentially the same. Generally, Stark components are well resolved and have been followed as a function of external field strength in increments of 0.1 V/cm. However, in Figs. 7 and 8 only every second spectrum is shown. The recorded linewidths range between 10 MHz, corresponding to our experimental resolution, and about 2–3 GHz. Dramatic variations in intensities, linewidths, and line shapes are observed when changing the applied field strength, in particular in the vicinity of avoided crossings, which are clearly visible when viewing Figs. 7 and 8 along the plane of paper. Because of the high density of states, many avoided crossings involve several Stark components simultaneously. A conspicuous example is provided by the crossing of four Stark components at $F\ge 97$ V/cm and relative energies $-15\le E\le -7.5$ GHz. Pronounced interference effects are observed at this multiple crossing since a broad, strongly autoionizing Stark component overlaps several quasibound Stark states. The variation of the photoionization cross section with energy and electric-field strength in the vicinity of this avoided crossing will be further analyzed in detail in the next section. The large number of avoided crossings can also be seen in Figs. 9 and 10, where we have plotted energies associated with maxima in experimental count rates and maxima in calculated photoionization cross sections versus applied electric-field strength. As before, energies are given relative to the zero-field energy of the $6s47d\,^1D_2$ Rydberg state. In Figs. 9 and 10 experimental and theoretical data (dots) have been connected to guide the eye. As can be seen from Figs. 9 and 10, good agreement between maximum ion count rates observed in experimental Ba Stark spectra and calculated maximum cross sections was obtained. In addition, the pattern of Figs. 9 and 10 closely resemble that of Fig. 6, i.e., there is almost a one-to-one correspondence between the variation of Stark components of hydrogen and barium with applied field strength. For example, the large areas devoid of any Stark components coincide in all figures.

Figure 11 provides a further illustrative example for the capability of the WKB-QD Stark theory in reproducing Stark spectra at high densities of states close to the classical field-ionization limit. In Fig. 11 we compare experimental (upper trace) and theoretical (lower trace) Stark spectra of barium over a wide range of energies but at fixed electric-field strength. The zero-field energy of the $6s50d\ ^1D_2$ barium Rydberg state has arbitrarily been chosen as origin of the frequency scale. In addition, zero-field energies of other $6snd\ ^1D_2$ ($n=46-51$) barium Rydberg states are indicated in Fig. 11. The spectra extend up to 445 GHz above the classical field-ionization limit ε_c, which is located at -345 GHz with respect to the origin of the frequency scale. At $E\approx-160$ GHz, the amplification of the counting electronics and the scaling factor of the numerical cross sections have been increased by a factor of 2, as indicated. In hydrogen about 260 Stark components are expected to fall in the energy range covered by Fig. 11 with principal quantum numbers ranging between $n=40$ and 53. At the external field strength of 97.88 V/cm the splitting between neighboring Stark components of a particular n multiplet is estimated (in linear approximation) to be $3Fn[(2\text{ Ry})/F_0]$, i.e., 15–20 GHz, whereas the total Stark splitting is approximately twice as large as the energy range spanned by Fig. 11. Because of the high density of states and the frequent avoided crossings, a designation of individual barium Stark components by hydrogenic parabolic quantum numbers is generally not possible. On the other hand the spectra are quasiperiodic over limited energy ranges, i.e.,

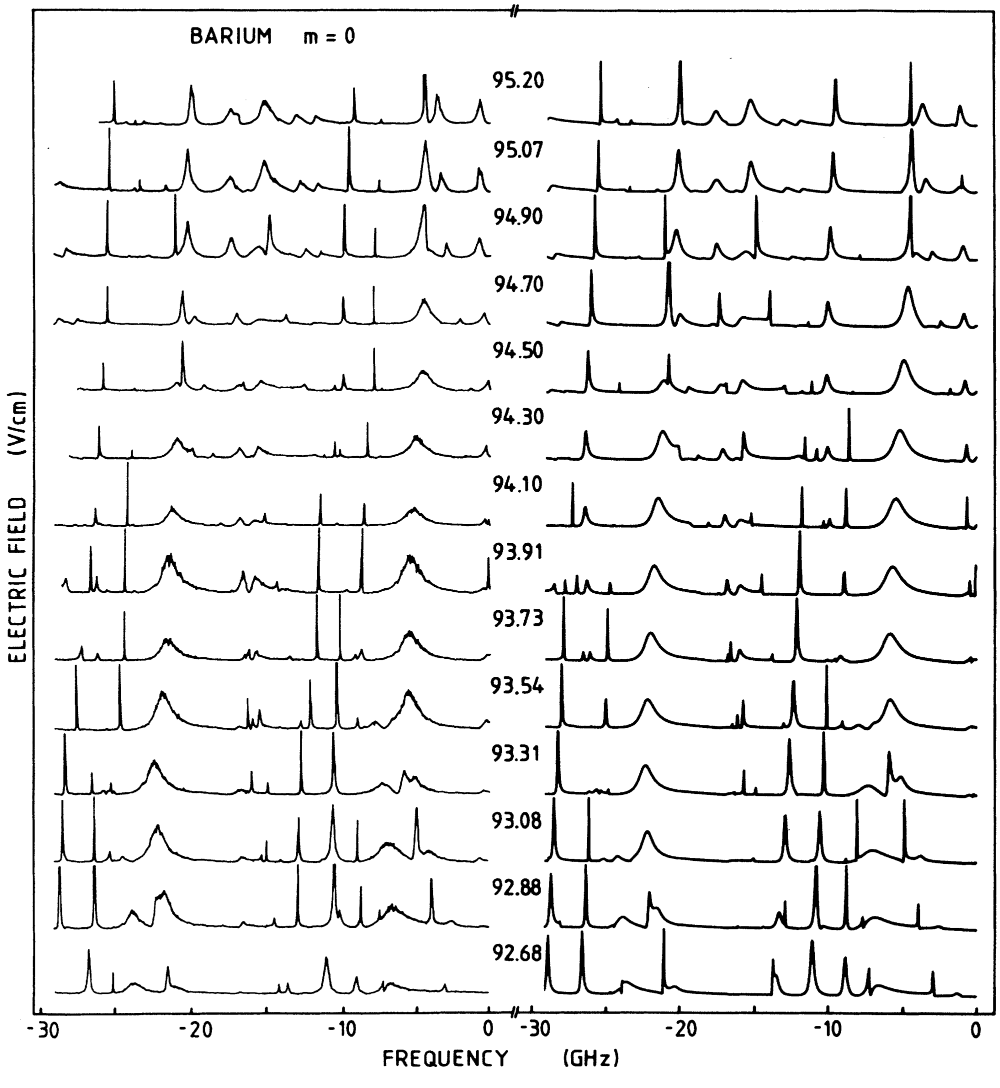

FIG. 7. Experimental (left-hand side) and calculated Stark spectra ($m=0$) of Ba, taken at different external field strengths ($92.68\leq F\leq 95.20$ V/cm). Frequencies are measured with respect to the zero-field energy of the $6s47d\ ^1D_2$ Rydberg state. One scaling factor common to all traces was used to facilitate comparison between experimental and theoretical spectra.

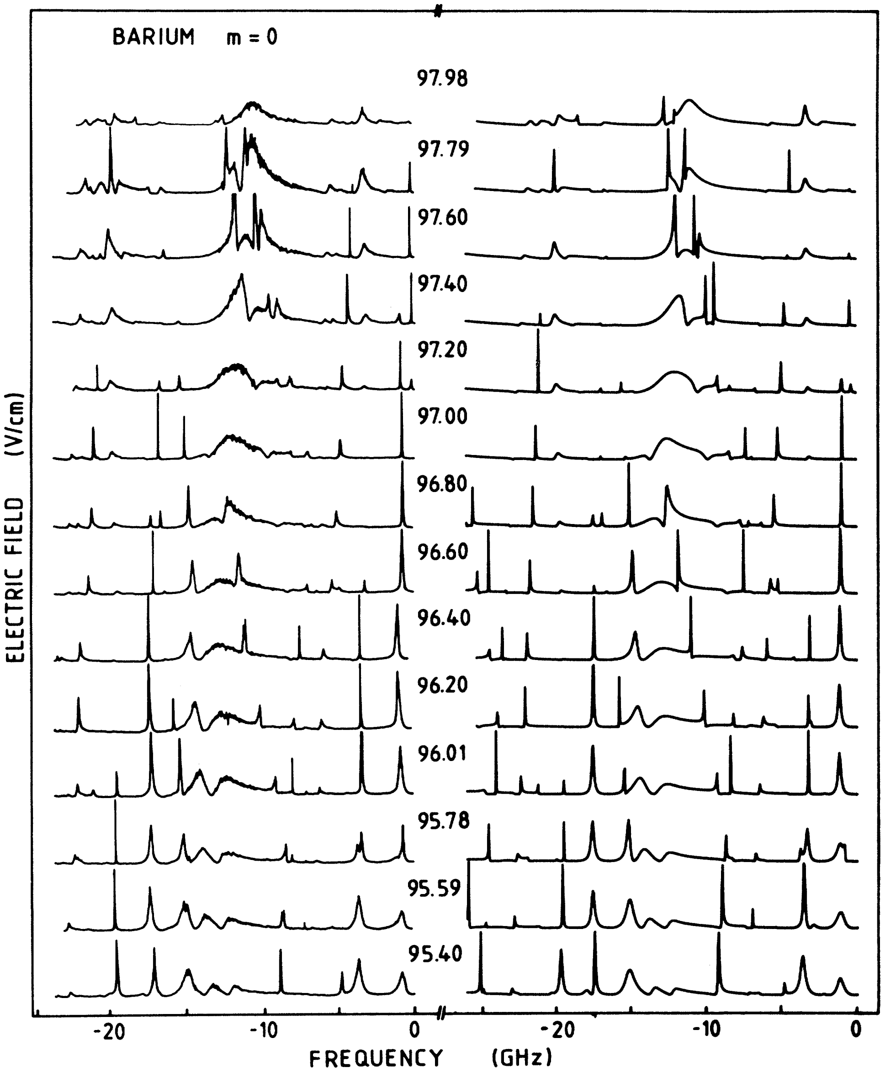

FIG. 8. Comparison of measured and calculated Stark spectra ($m = 0$) of barium extended to higher field strengths (see Fig. 7).

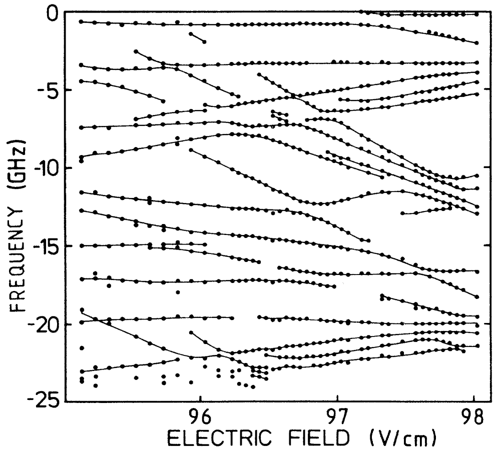

FIG. 9. Energies associated with peak ion count rates observed in spectra shown in Figs. 7 and 8. Experimental data (dots) have been connected to guide the eye. The frequency scales in Figs. 7–10 refer to the same origin.

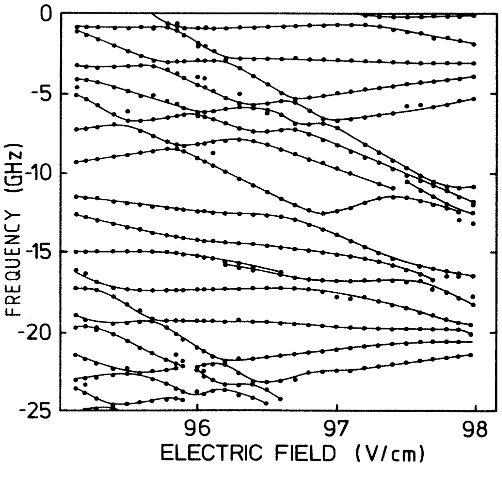

FIG. 10. Energies (dots) associated with maxima in theoretical photoionization cross sections illustrated in Figs. 7 and 8. See Fig. 9 for comparison with experimental data.

the overall appearance of the spectra is dominated by the linear Stark effect of adjacent Stark components belonging to one particular n multiplet. Because of the many avoided crossings between Stark components of different n multiplets, the linear Stark effect can be followed over limited energy ranges, only. This is particularly evident in the two lowermost traces of Fig. 11, where the strongly autoionizing Stark components appearing on the left-hand side between -45 and 27 GHz are approximately periodic. The same applies to the broad resonances on the right-hand side ($31 < E < 86$ GHz). The two series of resonances, exhibiting a splitting of $3Fn[(2\ \mathrm{Ry})/F_0]$; i.e. 18 GHz, are marked by corresponding arrows. There is an apparent break beyond the highest Stark component of the $n=43$ hydrogenic multiplet ($E=26$ GHz), indicated by the drop in intensities of narrow Stark components. In Fig. 11, a physically similar situation appears at lower energies and lower principal quantum numbers.

As can be seen from Figs. 7–11, excellent agreement was achieved between experimental and theoretical results, justifying the approximations made in applying the WKB-QD Stark theory. In particular, the calculated photoionization cross sections (Figs. 7, 8, and 11) reproduce all qualitative features observed experimentally. Apart from an energy-independent scaling factor for the calculated cross sections, the theoretical model contains no adjustable parameter. A common scaling factor was used for all spectra recorded under similar conditions, i.e., one factor for all spectra shown in Figs. 7 and 8 and another one for all traces of Fig. 11. Furthermore, all spectra were calculated with an energy resolution of 50 MHz, being insufficient for a complete resolution of the

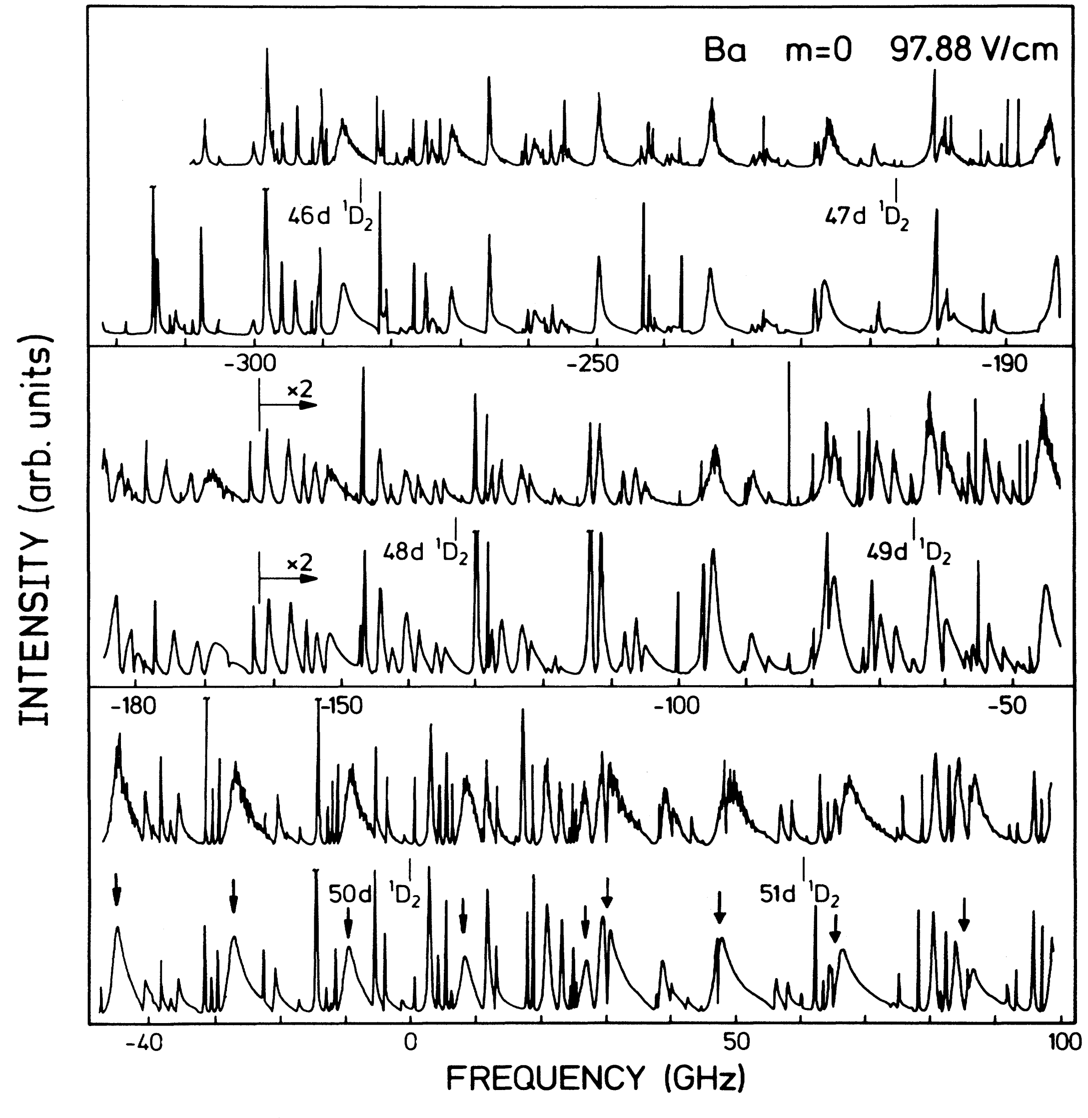

FIG. 11. Experimental (upper trace) and theoretical Stark spectra at constant electric-field strength. One constant scaling factor was used to adjust both vertical scales. Zero-field energies of $6snd\ ^1D_2$ Rydberg states are indicated. The frequency scale refers to the $n=50$ Rydberg state. In the lowermost trace two different series of adjacent, strongly autoionizing resonances with a Stark splitting of $3Fn[(2\ \mathrm{Ry})/F_0]$, i.e., 18 GHz, are marked by corresponding arrows.

narrowest Stark components observed. It follows from the discussion given in the preceding section that besides calculated hydrogenic matrices H^F and $\tilde{U}^F \cot\gamma_\beta^F U^F$, zero-field MQDT parameters have to be known for all bound Rydberg series. In barium, there are many doubly excited states perturbing bound $(6snl)$ Rydberg series because of the small energy separation between the lowest $({}^2S_{1/2}, {}^2D_{3/2}$, and ${}^2D_{5/2})$ ionization limits. Configuration interactions between barium Rydberg series with the same total angular momentum but converging towards different ionization limits cause off-diagonal elements in the corresponding zero-field K matrix. For our purposes, however, less information is necessary to calculate Stark spectra within the narrow energy range investigated experimentally. We have assumed all Rydberg series $6snl\,{}^1L_l$ with $l \geq 3$ to be hydrogenic, neglecting quantum defects of $6snf\,{}^1F_3$ $(\mu_3 = 0.047)$ and $6sng\,{}^1G_4$ $(\mu_4 = 0.059)$ Rydberg states.[17] Furthermore, no doubly excited states perturbing the $6sns\,{}^1S_0$ $(\mu_0 = 0.212)$, $6snp\,{}^1P_1$ $(\mu_1 = 0.149)$, and $6snd\,{}^1D_2$ $(\mu_2 = -0.290)$ Rydberg series are located in the energy range studied experimentally. It should be noted, however, that quantum defects of $6snp\,{}^1P_1$ Rydberg states appreciably vary with energy because of the perturbation of this series by the $5d8p\,{}^1P_1$ state, straddling the ionization limit.[18]. Therefore, we have taken an average over zero-field quantum defects of $6snp\,{}^1P_1$ states which effectively contribute to the wave functions of the Stark components observed. By using the experimentally derived quantum defects μ_l $(l \leq 2)$, given above, perturbations caused by doubly excited states outside the energy range under consideration are effectively taken into account. Hence, we can assume the barium ionic core to have effectively spherical symmetry. With the assumptions made above, the K matrix is diagonal, with only the first three elements being nonzero. In this way, the WKB-QD formulation of the Stark effect of nonhydrogenic atoms in its original form[12] can be used to analyze our barium data. In addition, we have generally neglected triplet states. This is justified because the $6s6p\,{}^1P_1$ state has almost pure singlet character. Therefore, transitions from this intermediate level to (pure) singlet and to (pure) triplet states have oscillator strengths differing by about 1 order of magnitude. It follows from Eqs. (9) and (10) that zero-field transition moments R_0^0 and R_2^0 are needed to calculate absorption cross sections for transitions to Ba $(m = 0)$ Stark components. By taking the ratio of transition probabilities $|\langle i|z|6s(n+1)s\,{}^1S_0\rangle / \langle i|z|6snd\,{}^1D_2\rangle|^2 = 0.09$, involving the $|i\rangle = |6s6p\,{}^1P_1\ m = 0\rangle$ intermediate level, from zero-field spectra, i.e., $(R_0^0)^2(2\,\mathrm{Ry}\nu_0^{-3})/(R_2^0)^2(2\,\mathrm{Ry}\nu_2^{-3}) = 0.09$, where $\nu_l = n - 3 - \mu_l$, we are able to calculate relative absorption cross sections without any adjustable parameters. In order to achieve agreement between calculated and experimental spectra, the relative sign of the transition moments is required to be positive.

In the remaining part of this paper we focus our attention on the analysis of a particular avoided crossing involving several Stark components. As mentioned above, a particularly interesting example is provided by the crossing of one strongly autoionizing (broad) Stark state with three narrow, effectively bound ones, observed for external field strengths between $F = 97.00$ and 97.98 V/cm and for relative energies $-15 \leq E \leq -7.5$ GHz (see Fig. 8). As can be seen from Fig. 6, these barium Stark states correspond to the hydrogenic components $(n = 41,\ n_1 = 38,\ n_2 = n - n_1 - 1 = 2)$ and (48,11,36), (49,9,39), and (51,6,44), respectively. The physical situation encountered at $F = 97.60$ V/cm is illustrated in Fig. 12. Besides experimental and theoretical barium Stark spectra (see Fig. 8) we show the contribution $D_{22}^F(\varepsilon)$ and the quantity $\det Q(\varepsilon)$ for comparison. Since the hydrogenic states are strongly bound, the linewidths and asymmetric line shapes of the barium Stark components are caused by autoionization due to core-induced continuum couplings, mentioned in the discussion of Fig. 4. In the vicinity of the avoided crossings, the linewidth of the component corresponding to the (41,38,2) hydrogenic Stark state exceeds the minimum energy splitting between the different Stark components because of the strong core-induced coupling. Hence, the line profile comprises narrow resonances due to the more strongly bound Stark levels and exhibits pronounced interference effects. Energies corresponding to hydrogenic resonances appear at the poles of the function $\det Q(\varepsilon)$, whereas barium Stark resonances occur when $\det Q(\varepsilon)$ vanishes.[19] Barium Stark resonances in the vicinity of isolated poles of $\det Q(\varepsilon)$ can be characterized by the parabolic quantum numbers of the corresponding hydrogenic state. The Stark shift due to the core-induced coupling is given by the difference in energies at which $\det Q(\varepsilon)$ vanishes and its (neighboring) pole appears. An example is provided by the Stark component at $E \approx -1$ GHz (see Fig. 12) being almost isolated, which can be identified with the zero and pole of $\det Q(\varepsilon)$ at about the same energy. In contrast, the many poles and zeros of $\det Q(\varepsilon)$ located in the range $-14 \leq E \leq -9$ GHz make such an identification impossible corresponding to strong mixing between barium Stark components. In addition, the linewidth of the barium Stark levels is proportional to the inverse of the slope of $\det Q(\varepsilon)$ at the resonance energy where $\det Q(\varepsilon)$ vanishes.[19] As can be seen from Fig. 12, the theoretical spectrum is dominated by the contribution D_{22}^F, reflecting the transition amplitudes to $6snd\,{}^1D_2\ m = 0$ components contributing to the final-state wave function. However, at certain energies (e.g., $E = -6$ GHz) differences between the total spectrum and the component D_{22}^F are observed and originate from contributions due to D_{00}^F and the interference term D_{02}^F, illustrated in Fig. 4. Despite the simplifying approximations made in applying the WKB-QD Stark theory, it provides an excellent description of our experimental spectra (see Figs. 7, 8, and 11).

B. Configuration-interaction analysis

Further physical insight is gained by analyzing the avoided crossing discussed in the preceding paragraph within the framework of configuration-interaction theory outlined earlier. Besides the four strongly closed channels forming the avoided crossing, we have included two additional bound ones, (50,7,42) and (46,16,29), in our configuration-interaction model. In Fig. 6, showing hy-

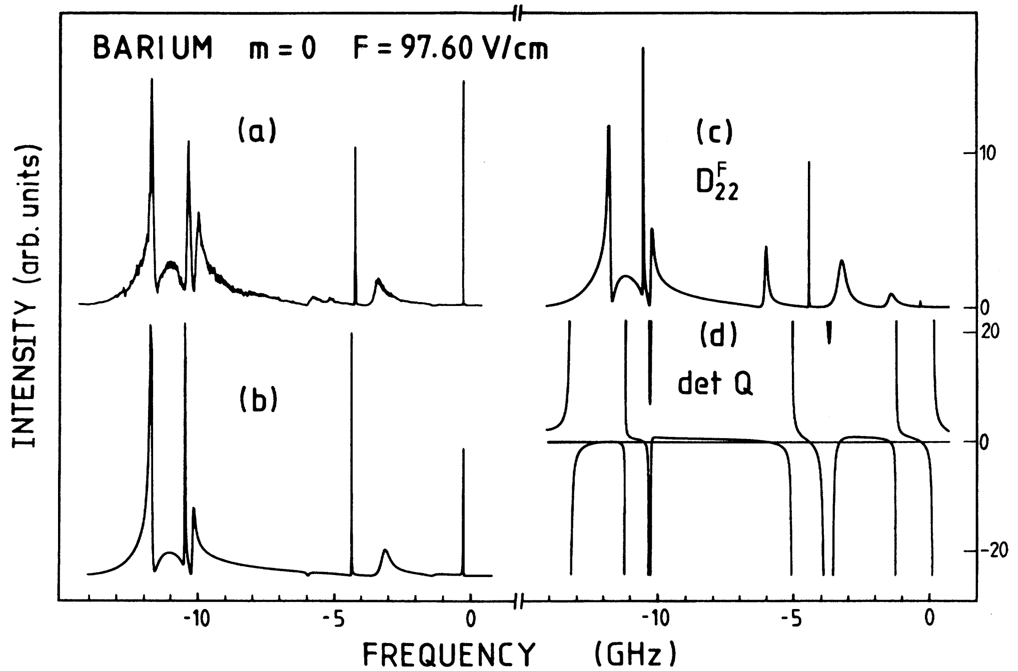

FIG. 12. Part of experimental (a) and theoretical (b) Stark spectrum at $F=97.60$ V/cm, also shown in Fig. 8, using the same scaling factor to facilitate comparison. Density-of-states matrix element D^F_{22} (c) and det$Q$ (d) [cf. Eq. (8)]. The origin of the frequency scale corresponds to the zero-field energy of the $6s47d\ ^1D_2$ Rydberg state. In (d) the horizontal line indicates det$Q=0$.

drogenic Stark energies, these channels appear about 5 GHz below the avoided crossing at $F=98$ V/cm, i.e., in the immediate vicinity of the avoided crossing under discussion. It should be noted that the channels (53,4,48) and (52,5,46) falling in between are open in this energy and electric-field range. In order to calculate the complex Hamiltonian matrix $h^c(\varepsilon)$, Fano q parameters, transition moments to modified bound states $(R_d)_i$ and the background amplitude $R_c(\varepsilon)\tilde{R}_c(\varepsilon)$ [cf. Eqs. (12) and (13)] employing the WKB-QD formalism, we have used the quantum defects μ_l $(0 \leq l \leq 2)$ and ratio of zero-field transition moments as previously. In addition, hydrogenic Stark energies ε_{n_1} were calculated at selected field strengths within the WKB approximation reported in Ref. 11. Stark energies for arbitrary field strengths within the range $97.00 \leq F \leq 98.50$ V/cm were obtained by linear interpolation. Furthermore, the hydrogenic Stark channels were assumed to be strongly bound, i.e., hydrogenic linewidths were set equal to zero. Since the configuration-interaction model uses state-normalized bound wave functions, renormalization of the WKB-QD wave functions is necessary. To this end, the slope $d\Delta/d\varepsilon$ of the WKB phase Δ was calculated at hydrogenic resonance energies ε_{n_1} for each n_1 channel.[12] This factor modifies the transformation from spherical to parabolic basis functions.

The right-hand side of Fig. 13 illustrates line profiles for different electric-field strengths $(97.10 \leq F \leq 97.98$ V/cm) associated with the avoided crossing calculated using Eq. (12). As can be seen by comparing theoretical line shapes and experimental spectra, good agreement was achieved despite the restricted model used. In order to facilitate this comparison, theoretical spectra were multiplied by a common scaling factor. As before, the zero-field energy of the $6s47d\ ^1D_2$ Rydberg state was chosen as origin of the frequency scale. In addition to the calculation of absorption cross sections according to Eq. (12), effective resonance energies [Fig. 14(a)] and linewidths [Fig. 14(b)] were obtained by diagonalizing the complex matrix h^c. The real part of the eigenvalues corresponds to effective resonance energies, whereas effective linewidths are given by twice the negative imaginary part. In Fig. 14(a) effective resonance energies measured with respect to the zero-field energy of the $6s47d\ ^1D_2$ Rydberg state have been plotted as a function of the external field strength. The upper part of Fig. 14(a) shows the group of four bound channels forming the avoided crossing under discussion, the effective linewidths of which are illustrated in Fig. 14(b) in logarithmic scale. In the upper part of Fig. 14(a) and in Fig. 14(b) the same symbols are used to designate the real and imaginary parts of a particular complex eigenvalue. The effective resonance energies of the two additional channels mentioned above are shown in the lower part of Fig. 14(a). As can be seen from Fig. 14(b) four minima in the effective linewidths caused by interference narrowing are observed for different channels at different electric-field strengths. Resonance energies corresponding to these minima are marked by crosses in Fig. 14(a). As can be seen, the minima in linewidths occur in the vicinity of avoided crossings of two channels. It should be noted, however, that line profiles cannot be calculated by reducing the avoided crossing involving all channels to a series of avoided crossings involving two channels only. The minima in linewidths correspond to conspicuously narrow resonances in the photoabsorption cross section. For example, at $F = 97.40$ V/cm, the minimum in linewidth is related to the bound channel with the second highest resonance energy [cf. Fig. 14(a)]. Correspondingly, a narrow resonance appears in the photoabsorption cross section (see Fig. 13) for the component of the line profile with the second highest energy at this particular external field strength. Because of the artificial separation of hydrogenic channels into closed and open ones, discontinuities in effective resonance energies and linewidths are observed. They appear when a closed hydrogenic channel exceeds its critical parabolic energy when increasing the external electric-field strength. A conspicuous example is provided by Fig. 14(b), where linewidths abruptly change at $F \approx 97.3$ V/cm, resulting from the opening of the hydrogenic channel (52,5,46). As discussed in Refs. 14 and 20, such discontinuities can be removed by replacing the summation over all open channels by a suitable integration.

Interference narrowing of Stark resonances has been observed previously in sodium by Liu *et al.*[9] and is caused by destructive interferences of decay amplitudes of bound channels to several commonly available continua. In a simple configuration-interaction model, two bound channels are coupled to two continua.[9] For each bound channel the continua can be prediagonalized. The occurrence of interference narrowing depends on the (normalized) overlap between those prediagonalized continua which couple to the corresponding discrete state. This overlap is expressed by the overlap angle γ (Refs. 9, 14, and 15), where $\cos\gamma = \Gamma_{12}/(\Gamma_{11}\Gamma_{22})^{1/2}$ can be expressed by the imaginary part of the complex off-diagonal element of h^c, i.e., $\Gamma_{12} = \sum_j V_{1j}\tilde{V}_{j2}$, normalized to the imaginary parts of the corresponding diagonal elements. As discussed in Ref. 9, a complete overlap of both decay channels ($\gamma = 0$) results in the decay of both bound chan-

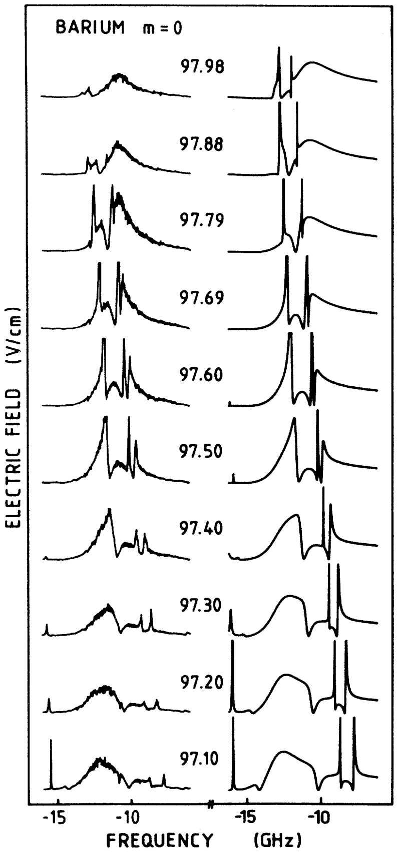

FIG. 13. Calculated (right-hand-side) and experimental Stark spectra at a multiple crossing of Stark components at different electric-field strengths. The spectra were calculated according to Eq. (12) with energy- and field-dependent parameters deduced from WKB-QD theory. Identical spectra were obtained with the parameters given in Table I. The origin of the frequency scale corresponds to the zero-field energy of the $6s47d\ ^1D_2$ Rydberg state. Experimental ion count rates and numerical cross sections have been adjusted using one common scaling factor.

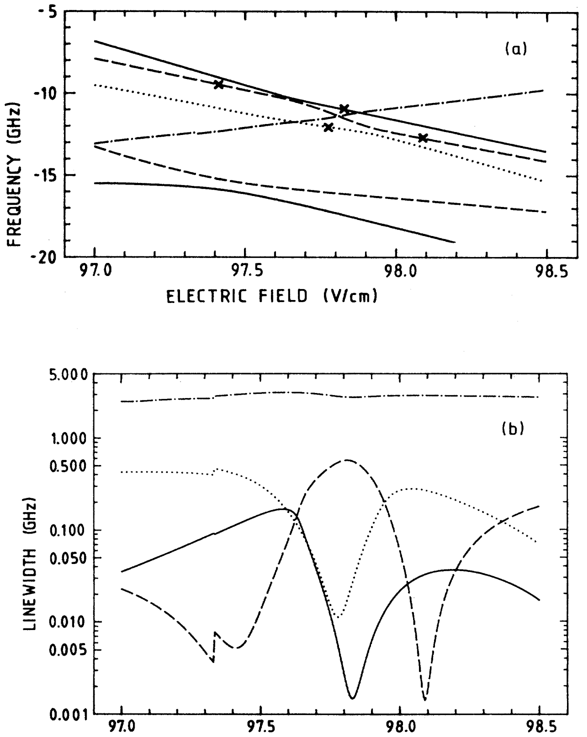

FIG. 14. Resonance energies (a) and linewidths (b) of Stark components at the multiple crossing shown in Fig. 13. The frequency scale of Fig. 14(a) refers to the zero-field energy of the $6s47d\ ^1D_2$ Rydberg state. At $F = 97$ V/cm the Stark components (from top to bottom) correspond to the hydrogenic (n, n_1, n_2) channels (51,6,44), (49,9,39), (48,11,36), (41,38,2), (50,7,42), and (46,16,29) (see Fig. 6). (b) includes the four upper components of (a) only, using the same designation. The crosses in (a) indicate the four interference minima observed in (b).

TABLE I. Field-independent parameters of configuration-interaction model for approximate description of multiple crossing shown in Fig. 13. Core-induced elements of the Hamiltonian matrix h^c, dipole transition matrix elements $(R_d)_{n_1}$, normalized to the zero-field transition matrix element $\langle 6s6p\,^1P_1\ m=0|z|6s47d\,^1D_2\ m=0\rangle$, and Fano q parameters q_{n_1} are given.

n_1	6	7	9	11	16	38
$(h^c)_{n_1' n_1}$ (GHz)	$-0.18-(i/2)0.02$	$-0.23-(i/2)0.04$	$-0.29-(i/2)0.06$	$-0.34-(i/2)0.08$	$+0.43-(i/2)0.13$	$+0.43+(i/2)0.18$
		$-0.28-(i/2)0.06$	$-0.33-(i/2)0.11$	$-0.37-(i/2)0.15$	$-0.42-(i/2)0.23$	$+0.32+(i/2)0.35$
			$-0.34-(i/2)0.18$	$-0.34-(i/2)0.25$	$-0.31-(i/2)0.39$	$-0.04+(i/2)0.60$
				$-0.30-(i/2)0.35$	$-0.20-(i/2)0.56$	$-0.40+(i/2)0.87$
					$+0.07-(i/2)0.88$	$-1.26+(i/2)1.38$
						$+0.63-(i/2)2.19$
$(R_d)_{n_1}$	0.56	0.49	0.19	-0.10	-0.74	2.65
q_{n_1}	-5.6	-2.6	$-.60$	.22	1.0	2.3

nels into one mixed, prediagonalized continuum only. This causes the linewidth of one of the bound channels to vanish at a particular value of the external electric-field strength in the vicinity of the avoided crossing. As mentioned above, however, the avoided crossing involving four bound Ba Stark states cannot be analyzed in terms of isolated avoided crossings of two states, i.e., the complex matrix h^c cannot be broken down into several 2×2 matrices.

Because of the narrow energy and electric-field range under consideration, parameters entering our configuration-interaction model can be taken as being approximately independent of energy and electric-field strength. In particular, the background amplitude $R_c(\varepsilon)\tilde{R}_c(\varepsilon)$, the transition moments $(R_d)_i$ between the initial ($6s6p\,^1P_1\ m=0$) state, and the six (modified) bound states as well as the Fano parameters q_i are taken as energy and field independent. The same applies to the complex matrix $h^c(\varepsilon)$ except for the contribution of hydrogenic Stark energies ε_{n_1} to the real parts of its diagonal elements. As mentioned above, these hydrogenic resonance energies were interpolated linearly between different electric-field strengths. In Table I we list the core-induced parts of the complex matrix h^c only, i.e., the matrix elements $(h^c)_{n_1' n_1}-\varepsilon_{n_1}\delta_{n_1' n_1}$. In addition, the transition moments $(R_d)_{n_1}$, normalized to the zero-field transition matrix element

$$\langle 6s6p\,^1P_1\ m=0|z|6s47d\,^1D_2\ m=0\rangle = R_2^0[(2\ \mathrm{Ry})\nu_2^{-3}]^{1/2}$$

and the Fano parameters q_{n_1} are given. The background amplitude $R_c\tilde{R}_c$, normalized to

$$|\langle 6s6p\,^1P_1\ m=0|z|6s47d\,^1D_2\ m=0\rangle|^2\ ,$$

was inferred from Eq. (13) to be 0.41, using the parameters given in Table I. By diagonalizing the complex matrix h^c, using the energy- and field-independent parameters given in Table I, line profiles essentially identical to those shown in Fig. 13 have been obtained. The diagonal elements given in Table I correspond to core-induced energy shifts relative to the hydrogenic resonance energies ε_{n_1} and core-induced linewidths $\Gamma_{n_1 n_1}$ of isolated resonances. Likewise, the Fano q parameters of Table I relate to isolated resonances. While this situation can be constructed as an asymptotic limit within the six-channel model, this situation is not realized in nature because of the high density of states in the energy and electric-field range under consideration. However, the line profiles shown in Fig. 13 can be reproduced by coherent superposition of these isolated Fano-Beutler profiles using Eq. (12) and by varying only hydrogenic resonance energies with external field. Furthermore, because of the large imaginary parts $\Gamma_{n_1' n_1}$ associated with the state (41,38,2), the real parts of the complex eigenvalues of h^c tend to cross [see Fig. 14(a)] when this channel contributes significantly to the eigenstates. A different physical situation was encountered by Liu *et al.*[9] at the crossing of the sodium Stark components (20,19,0) and (21,17,3) at $F=3950$ V/cm. Within a two-channel model, resonance energies (real parts of complex eigenvalues) anticross, whereas linewidths (imaginary parts) cross exactly. Conditions for the crossing and anticrossing of resonance energies and linewidths have been discussed recently by McNicholl *et al.*[14]

In conclusion, we have recorded high-resolution Stark spectra of barium Rydberg states at a high density of states close to the field-ionization limit. The spectra were successfully analyzed employing the WKB-QD Stark theory,[12] taking three nonvanishing quantum defects μ_l ($0\le l\le 2$) into account only and neglecting doubly excited configurations. Our measurements provide a test of the WKB-QD theory in an energy and electric-field range, where core-induced coupling between closed and open Stark channels provides the dominant decay mechanism. In addition, strongly field-dependent line profiles observed at a particular multiple crossing of Stark components were parameterized within a configuration-interaction model whose parameters were calculated employing a reformulation[14] of the WKB-QD theory. Several interference minima in the linewidths deduced for Stark components involved in this multiple crossing were observed at different external field strengths.

V. ACKNOWLEDGMENTS

This work was supported by the Deutsche Forschungsgemeinschaft (DFG), Sonderforschungbereich 161 (Hyperfeinwechselwirkungen) and through DFG Grant No. Ri 378/1. One of us (A.K.) gratefully acknowledges the receipt of a grant from the Senate of Berlin. We thank Dr. T. Bergeman for sending us his manuscript on the reformulation of the WKB-QD theory prior to publication and for his advice. The help of M. Kohl, H.-J. Grabka, and K. Vietzke in performing the experiments is acknowledged.

---

[*] Present address: Physikalisch-Technische Bundesanstalt, Institut Berlin, Abbestrasse 2-12, 1000 Berlin 10, Germany.

[1] See, for example, *Atomic Excitation and Recombination in External Fields,* edited by M. H. Nayfeh and C. W. Clark (Gordon and Breach, New York, 1985).

[2] M. L. Zimmerman, M. G. Littman, M. M. Kash, and D. Kleppner, Phys. Rev. A **20**, 2251 (1979); S. Liberman and J. Pinard, Phys. Rev. *ibid.* **20**, 507 (1979); E. Luc-Koenig, S. Liberman, and J. Pinard, *ibid.* **20**, 519 (1979).

[3] R. R. Freeman and G. C. Bjorklund, Phys. Rev. Lett. **40**, 118 (1978).

[4] E. B. Saloman, J. W. Cooper, and D. E. Kelleher, Phys. Rev. Lett. **55**, 193 (1985).

[5] R. R. Freeman, N. P. Economou, G. C. Bjorklund, and K. T. Lu, Phys. Rev. Lett. **41**, 1463 (1978); M. G. Littman, M. M. Kash, and D. Kleppner, *ibid.* **41**, 103 (1978).

[6] T. S. Luk, L. DiMauro, T. Bergeman, and H. Metcalf, Phys. Rev. Lett. **47**, 83 (1981).

[7] S. Feneuille, S. Liberman, J. Pinard, and A. Taleb, Phys. Rev. Lett. **42**, 1404 (1979).

[8] W. van de Water, D. R. Mariani, and P. M. Koch, Phys. Rev. A **30**, 2399 (1984).

[9] J.-Y. Liu, P. McNicholl, D. A. Harmin, J. Ivri, T. Bergeman, and H. J. Metcalf, Phys. Rev. Lett. **55**, 189 (1985).

[10] S. Feneuille, S. Liberman, E. Luc-Koenig, J. Pinard, and A. Taleb, J. Phys. B **15**, 1205 (1982); P. McNicholl, T. Bergeman, and H. J. Metcalf, Phys. Rev. A **37**, 3302 (1988).

[11] D. A. Harmin, Phys. Rev. A **24**, 2491 (1981); E. Luc-Koenig and A. Bachelier, Phys. Rev. Lett. **43**, 921 (1979); J. Phys. B **13**, 1743 (1980); **13**, 1769 (1980).

[12] D. A. Harmin, Phys. Rev. A **26**, 2656 (1982); Phys. Rev. Lett. **49**, 128 (1982).

[13] D. A. Harmin, Comm. At. Mol. Phys. **15**, 281 (1985); K. Sakimoto, J. Phys. B **19**, 3011 (1986).

[14] P. McNicholl, J. Ivri, and T. Bergeman (unpublished).

[15] U. Fano, Phys. Rev. **124**, 1866 (1961); F. H. Mies, *ibid.* **175**, 164 (1968).

[16] A. Nussenzweig, E. E. Eyler, T. Bergeman, and E. Pollack, Phys. Rev. A **41**, 4944 (1990).

[17] J. Neukammer, G. Jönsson, A. König, K. Vietzke, H. Hieronymus, and H. Rinneberg, Phys. Rev. A **38**, 2804 (1988).

[18] J. A. Armstrong, J. J. Wynne, and P. Esherick, J. Opt. Soc. Am. **69**, 211 (1979).

[19] D. A. Harmin, Phys. Rev. A **30**, 2413 (1984).

[20] D. A. Harmin, in Ref. 1.